Atmosphere-like turbulence generation with surface-etched phase-screens

Stefan Hippler, Felix Hormuth, David J. Butler, Wolfgang Brandner, and Thomas Henning

Max-Planck-Institut für Astronomie
Königstuhl 17, D-69117 Heidelberg, Germany

hippler@mpia.de

http://www.mpia.de

Abstract: We built and characterized an optical system that emulates the optical characteristics of an 8m-class telescope like the Very Large Telescope. The system contains rotating glass phase-screens to generate realistic atmosphere-like optical turbulence, as needed for testing multi-conjugate adaptive optics systems. In this paper we present an investigation of the statistical properties of two phase-screens etched on glass-plate surfaces, obtained from Silios Technologies. Those etched screens are highly transmissive (above 85%) from 0.45 to 2.5 μm. From direct imaging, their Fried parameter r_0 values (0.43 ± 0.04 mm and 0.81 ± 0.03 mm, respectively, at 0.633μm) agree with the expectation to within 10%. This is also confirmed by a comparison of measured and expected Zernike coefficient variances. Overall, we find that those screens are quite reproducible, allowing sub-millimetre r_0 values, which were difficult to achieve in the past. We conclude that the telescope emulator and phase-screens form a powerful atmospheric turbulence generator allowing systematic testing of different kinds of AO instrumentation.

OCIS codes: (010.1080) Adaptive optics; (010.1330) Atmospheric turbulence

---

References and links

1. A. Kolmogorov, "The local structure of turbulence in incompressible viscous fluids at very large Reynolds numbers," Dokl. Akad. Nauk. SSSR **30**, 301–305 (1941). Reprinted in: S.K. Friedlander and L. Topper (editors). 1961. Turbulence: Classic Papers on Statistical Theory, Interscience Publications, New York, pp. 151-155.

2. V. I. Tatarskii and V. U. Zavorotny, "Atmospheric turbulence and the resolution limits of large ground-based telescopes: comment," J. Opt. Soc. Am. A **10**, 2410–2414 (1993).

3. J.-M. Conan, G. Rousset, and P.-Y. Madec, "Wave-front temporal spectra in high-resolution imaging through turbulence," J. Opt. Soc. Am. A **12**, 1559–1570 (1995).

4. A. Weiß, S. Hippler, M. Kasper, N. Wooder, and J. Quartel, "Simultaneous measurements of the Fried parameter r_0 and the isoplanatic angle θ_0 using SCIDAR and adaptive optics - First results," in *ASP Conf. Ser. 266: Astronomical Site Evaluation in the Visible and Radio Range*, J. Vernin, Z. Benkhaldoun, and C. Muñoz-Tuñón, eds., pp. 86–+ (2002).

5. T. Berkefeld, A. Glindemann, and S. Hippler, "Multi-Conjugate Adaptive Optics with Two Deformable Mirrors - Requirements and Performance," Exp. Astron. **11**, 1–21 (2001).

6. E. Marchetti, N. N. Hubin, E. Fedrigo, J. Brynnel, B. Delabre, R. Donaldson, F. Franza, R. Conan, M. Le Louarn, C. Cavadore, A. Balestra, D. Baade, J.-L. Lizon, R. Gilmozzi, G. J. Monnet, R. Ragazzoni, C. Arcidiacono, A. Baruffolo, E. Diolaiti, J. Farinato, E. Vernet-Viard, D. J. Butler, S. Hippler, and A. Amorin, "MAD the ESO multi-conjugate adaptive optics demonstrator," in *Adaptive Optical System Technologies II. Edited by Wizinowich, Peter L.; Bonaccini, Domenico. Proceedings of the SPIE, Volume 4839, pp. 317-328 (2003).*, P. L. Wizinowich and D. Bonaccini, eds., pp. 317–328 (2003).

7. A. Tokovinin, "Seeing Improvement with Ground-Layer Adaptive Optics," PASP **116**, 941–951 (2004).

8. R. Koehler, S. Hippler, M. Feldt, R. Gratton, D. Gisler, R. Stuik, and J. Lima, "Optimizing wavefront sensing for extreme AO," in *Advancements in Adaptive Optics. Edited by Domenico B. Calia, Brent L. Ellerbroek, and Roberto Ragazzoni. Proceedings of the SPIE, Volume 5490, pp. 586-592 (2004).*, D. Bonaccini Calia, B. L. Ellerbroek, and R. Ragazzoni, eds., pp. 586–592 (2004).

9. R. Ragazzoni, E. Diolaiti, J. Farinato, E. Fedrigo, E. Marchetti, M. Tordi, and D. Kirkman, "Multiple field of view layer-oriented adaptive optics. Nearly whole sky coverage on 8 m class telescopes and beyond," A&A **396**, 731–744 (2002).

10. B. Neichel, T. Fusco, M. Puech, J.-M. Conan, M. Lelouarn, E. Gendron, F. Hammer, G. Rousset, P. Jagourel, and P. Bouchet, "Adaptive Optics Concept For Multi-Objects 3D Spectroscopy on ELTs," astro-ph **0512525** (2005).

11. D. J. Butler, E. Marchetti, J. Baehr, W. Xu, S. Hippler, M. E. Kasper, and R. Conan, "Phase screens for astronomical multi-conjugate adaptive optics: application to MAPS," in *Adaptive Optical System Technologies II. Edited by Wizinowich, Peter L.; Bonaccini, Domenico. Proceedings of the SPIE, Volume 4839, pp. 623-634 (2003).*, P. L. Wizinowich and D. Bonaccini, eds., pp. 623–634 (2003).

12. D. Butler, S. Hippler, S. Egner, W. Xu, and J. Baehr, "Broadband, static wave-front generation: Na-AG ion-exchange phase screens and telescope simulation," Appl. Opt. **43**, 2813–2823 (2004).

13. S. Hippler, F. Hormuth, W. Brandner, D. Butler, T. Henning, and S. Egner, "The MPIA multipurpose laboratory atmospheric turbulence simulator MAPS," in *Advances in Adaptive Optics II. Proceedings of the SPIE, Volume 6272* (2006).

14. V. A. Klueckers, N. J. Wooder, T. W. Nicholls, M. J. Adcock, I. Munro, and J. C. Dainty, "Profiling of atmospheric turbulence strength and velocity using a generalised SCIDAR technique," A&A Supplement **130**, 141–155 (1998).

15. A. Fuchs, M. Tallon, and J. Vernin, "Focusing on a Turbulent Layer: Principle of the "Generalized SCIDAR"," PASP **110**, 86–91 (1998).

16. D. L. McKenna, R. Avila, J. M. Hill, S. Hippler, P. Salinari, P. C. Stanton, and R. Weiss, "LBT facility SCIDAR: recent results," in *Adaptive Optical System Technologies II. Edited by Wizinowich, Peter L.; Bonaccini, Domenico. Proceedings of the SPIE, Volume 4839, pp. 825-836 (2003).*, P. L. Wizinowich and D. Bonaccini, eds., pp. 825–836 (2003).

17. R. Avila, E. Carrasco, F. Ibañez, J. Vernin, J.-L. Prieur, and D. X. Cruz, "Generalized SCIDAR Measurements at San Pedro Mártir. II. Wind Profile Statistics," PASP **118**, 503–515 (2006).

18. S. Egner, E. Mascidari, D. McKenna, T. M. Herbst, and W. Gaessler, "G-SCIDAR measurements on Mt. Graham: recent results," in *Advances in Adaptive Optics II. Proceedings of the SPIE, Volume 6272* (2006).

19. J. Kolb, E. Marchetti, S. Tisserand, F. Franza, B. Delabre, F. Gonte, R. Brast, S. Jacob, and F. Reversat, "MAPS: a turbulence simulator for MCAO," in *Advancements in Adaptive Optics. Edited by Domenico B. Calia, Brent L. Ellerbroek, and Roberto Ragazzoni. Proceedings of the SPIE, Volume 5490, pp. 794-804 (2004).*, D. Bonaccini Calia, B. L. Ellerbroek, and R. Ragazzoni, eds., pp. 794–804 (2004).

1. Introduction

The optical image quality and in particular the angular resolution of ground based telescopes is hampered by the refractive index variations of the Earth's atmosphere. These refractive index variations show a temporal and spatial behavior that under certain assumptions is well described by Kolmogorov turbulence [1, 2, 3].

Adaptive optics (AO) instrumentation, available on almost all 8–10m-class telescopes, can compensate for optical turbulence (seeing) with certain restrictions. One of these restrictions is the isoplanatic angle, which is a result of using a single reference star for the AO and therefore compensating the integral effect of atmospheric turbulence in one direction only. Multi-conjugate AO systems that compensate the dominant turbulent layers instead, can increase the isoplanatic angle from a few tens of arcseconds [4] to up to a few arcminutes at $2.2\,\mu$m [5].

With the advent of second generation AO systems like multi-conjugate AO [6], ground layer AO [7], extreme AO [8], multiple field of view AO [9], and multiple object AO [10], it is becoming more and more important to have a realistic 3D turbulence simulation tool available in the laboratory. Such a tool provides repeatable optical turbulence and therefore well defined atmospheric conditions. It can support the assembly, integration, and verification phase of novel AO instrumentation such that AO performance can be verified before the instrument is attached to the telescope.

In our previous papers [11, 12] we described the design, manufacturing process, and lab-

oratory characterization of ion-exchange phase-screens. While such phase-screen technology allows repeatable optical turbulence generation over a wide spectral range, 0.5–2.5μm, it does not allow sub-millimetre r_0 values. In this paper we focus on a new type of phase-screen, based on transmissive glass substrates with aberrations imprinted on one surface. The motivation for investigating this new technique is this: For laboratory characterization of astronomical adaptive optics systems designed for D=8–40-m-class telescopes, D/r_0 values greater 30 are required. As we can only use scaled-down telescope optics in a laboratory, with typical values of D_{lab}=10 mm, we need r_0 values smaller than D_{lab}/30=1/3 mm. Glass phase screens with such small r_0 values were in the past difficult to fabricate. We identified the surface etching technique as the only tool and therefore best solution so far to this problem.

In the following, we firstly describe in Sec. 2 the design of MAPS, an optical set-up used to test the screens. The design and manufacture of the screens is then outlined in Sec. 3. Our analyses and results are presented in Sec. 4, and we briefly summarize our findings in Sec. 5.

2. MAPS, the multi atmospheric phase-screens and stars instrument for the visible and near-infrared

MAPS is a laboratory tool that allows simulation of 3D atmospheric optical turbulence over a wide field of view up to 2 arcminutes. It consists of 3 main components. A plate for light sources, comprising 34 fiber connectors [13] to investigate wide field wavefront reconstruction for various artificial-star configurations. The second main part of the MAPS design [11] consists of two optical tubes containing identical groups of lenses, fabricated by Janos Technology, Inc., Keene, NH, USA. The first tube collimates the point sources of the reference plate and creates the telescope pupil. The second tube refocuses the disturbed light beams into a 2 arcminute-wide focal plane with the optical characteristics of the Very Large Telescope (VLT) f/15 Nasmyth focus. The third main component of MAPS is a set of phase-screens. Up to 3 glass phase-screens can be mounted in between the two optical tubes. When rotating, those screens emulate a turbulent atmosphere consisting of a ground or boundary layer, a mid-altitude layer, and a high altitude layer. Each glass-plate can rotate with an adjustable and reproducible speed to emulate different atmospheric wind speeds per layer (see also [12]). Additionally, we can adjust the position of each glass-plate along the optical axis of the system to emulate atmospheric layers at different altitudes. Such a layered approach of atmospheric turbulence is supported by a number of experimental studies [14, 15, 4, 16, 17, 18].

The glass-plate phase-screen design was kindly provided by ESO [19]. The telescope pupil of MAPS is implemented through a 13 mm (equivalent to an 8-m telescope) pupil stop installed immediately behind the ground layer phase-screen when viewed from the direction of the collimating lens assembly.

3. Fabricating the surface etched phase-screens

3.1. Phase-screen phase maps

The phase maps of the phase-screens manufactured for the MAPS assembly are shown in Fig. 1. In the following the screens will be denoted as PS1 and PS2, with PS1 being the more turbulent screen. PS1 is used as the ground layer screen in the final MAPS assembly, while PS2 will be used as the mid- or high-layer screen. The peak-to-valley differences of the phase maps are 7.9 and 5.5μm, respectively. One pixel of the phase map corresponds to 0.1mm on the manufactured screen.
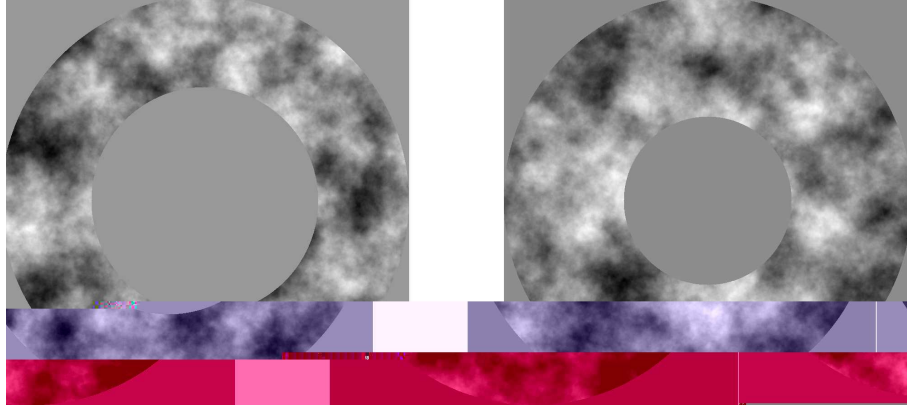
Fig. 1. Phase maps of the ground layer phase-screen PS1 (left) and mid- to high-altitude phase-screen PS2 (right).

3.2. *Fused silica substrate*

The glass-plate phase-screens from Silios Technologies, France, are manufactured with a wet etch process based on hydrochloric acid. The equipment is similar to standard semiconductor processing equipment used for 4-inch wafers. The phase pattern is etched into the 100 mm diameter and 1.5 mm thick glass substrate consisting of fused silica (Corning code 7980) from Corning Inc., USA. This high purity amorphous silicon dioxide has a very good transmission in the required spectral range from 0.5–2.5 μm. As shown in Fig. 2 the transmission is >90% over the entire spectral range with only two small H_2O-absorption features at around 1.4 and 2.2 μm. Visual inspection of the screens does not reveal any inhomogeneities or opaque patches. The phase-screens are realized through a multilevel profile created with either 5 (PS2) or 6 (PS1) masks, which eventually lead to 2^5=32 and 2^6=64 different levels of the phase map.
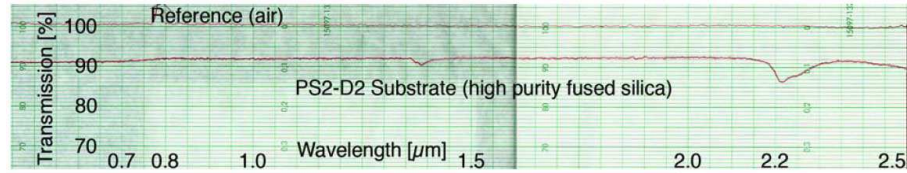

Fig. 2. Transmission in % as a function of wavelength, measured for phase-screen PS2.

4. Characterization of glass-plate phase-screens from Silios Technologies

For the (statistical) characterization of the manufactured phase-screens we use two different approaches: first, methods based on measurements of the point spread function (PSF), and second, wavefront-based methods. The basic parameter we wanted to measure and compare to the theoretical expectation, is the well-known Fried parameter r_0. An equally important quantity is the slope of the turbulence power spectrum or the slope of the variance of the Zernike coefficients vs. mode number. Although these quantities could be readily derived in the case of the available computer-generated template wavefronts used for the phase-screens, characterizing the power
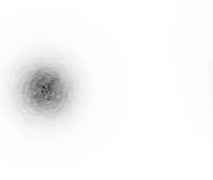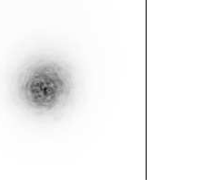
	Short exposure Point Spread Functions		Long exposure Point Spread Functions	
	632.8nm	831.5nm	632.8nm	831.5nm
PS1				
PS2				

Fig. 3. Four representative images of both short- and long-exposure point spread functions for PS1 and PS2, at 632.8nm and 831.5nm. The data was taken using an aperture size of 13mm. The size of each image is 200x200 CCD pixel^2.

spectrum of the manufactured screens requires an accurate measurement of the actual distorted wavefront.

4.1. Point spread function (PSF) measurement

To measure the PSF we put a single phase-screen at the ground layer position in the MAPS assembly, using a 13mm pupil-stop as the telescope aperture, which is equivalent to a real-world aperture of 8m. A single-mode fiber at the center of the field of view on the input side of MAPS was used as light source. Measurements were performed at two wavelengths, using a HeNe laser with λ=632.8nm, and a diode laser with λ=831.5nm. A standard CCD with a pixel size of 6.9x6.9 μm^2 was placed in the focal plane of the imaging side to record PSF images. To capture short exposure PSFs, the phase-screen was rotated at a speed of typically 0.5 rpm, while the CCD acquired large sets of exposures (of the order of several thousand) with integration times of a few milliseconds. Afterwards, all short exposure images were stacked to generate the long exposure PSF image used for the coherence length (r_0) measurement. In Fig. 3 we show examples of short and long exposure PSFs for both phase-screens at the two wavelengths. In order to derive values for r_0 we additionally took images using pinholes of different sizes as telescope aperture and recorded the resulting PSFs without a phase-screen in the optical beam.

The FWHM of the PSF obtained without any turbulence – the diffraction limited PSF – is then given by:

$$FWHM_{DL} = 1.02 \cdot \frac{\lambda}{D} \cdot S, \tag{1}$$

where the subscript DL denotes the diffraction limited FWHM, and D is the diameter of the pupil-stop defining the telescope aperture. The factor S is the image scaling factor of our system, containing both focal length and pixel size and determined with the calibration images. Our calibration measurements are in agreement with the predicted λ/D behavior within the measurement errors. For the FWHM measured in radians and the telescope diameter given in meters, S would be simply unity. Knowing the value for S we are able to compute the coherence length r_0 from the measured FWHM of our seeing limited long exposure PSFs (FWHM$_{SL}$)

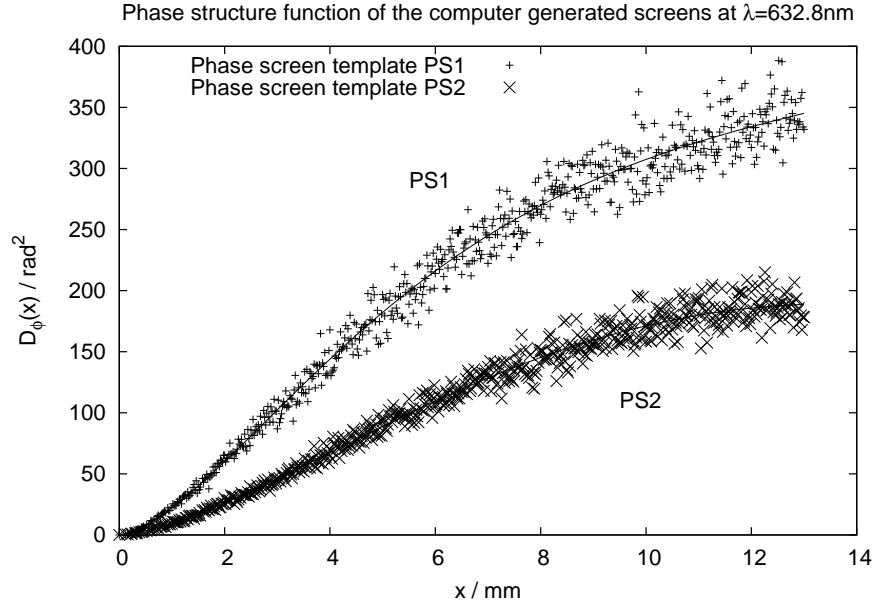Phase structure function of the computer generated screens at λ=632.8nm

Fig. 4. Phase structure function of the computer generated screens for a wavelength of 632.8nm (optical phase differences scaled to this wavelength, calculated on 360 randomly selected apertures of 13mm diameter with 10^6 point pairs in each). The solid lines represent a fit with L_0=22m and the values of r_0 as listed in Tbl. 1

using the equation:

$$r_0 = 0.98 \cdot \frac{\lambda}{FWHM_{SL}} \cdot S \tag{2}$$

Before giving the actual results of these measurements, we first describe how we derived r_0 in the case of the computer-generated template wavefronts. In a first step we reconstructed the phase structure function described by

$$D_\Phi(x) = < [\Phi(x') - \Phi(x' + x)]^2 > . \tag{3}$$

The resulting structure functions of both screens are shown in Fig. 4. It is well visible that the structure function indeed flattens out at larger values of x, clearly indicating a finite outer scale L_0. An outer scale of L_0=22m – typical for the Paranal observatory – was assumed for the design of the phase maps, and the measured flattening of the phase structure function is compatible with this value.

In a second step we used the phase structure function to compute the optical transfer function (OTF) of the phase-screens using the equation

$$OTF(x) = \exp[-0.5 D_\Phi(x)]. \tag{4}$$

Since the PSF is the inverse Fourier transform of the OTF we are able to directly compute the long exposure PSFs of our phase-screen computer templates, and to compare them with our experimental results for the manufactured screens. In Fig. 5 we show the theoretically expected PSFs, scaled to the measurement wavelengths and the image scale of our set-up, together with
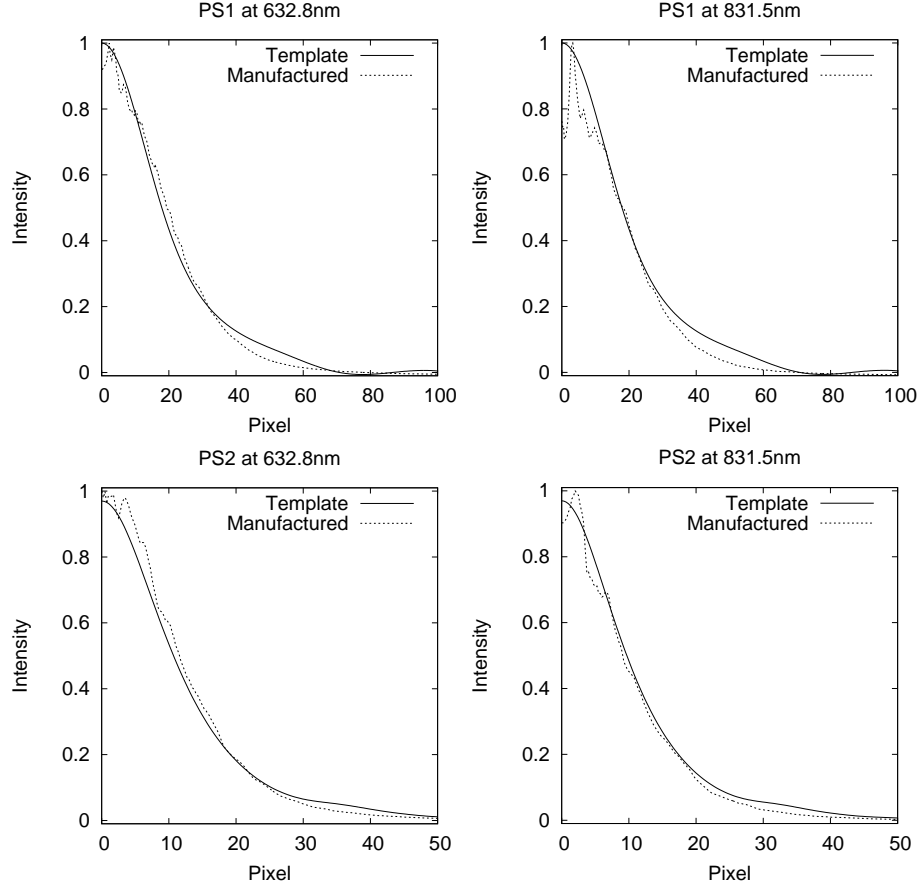
Fig. 5. Demonstrating the close agreement between the expected (Template) and measured (Manufactured) long exposure PSFs for phase-screen PS1 (upper row) and PS2 (lower row). Shown are the normalized radial intensity profiles at λ=632.8nm (left column) and λ=831.5nm (right column). Please note the different ranges of the abscissa.

the radially averaged and normalized profiles of the PSFs measured from direct imaging. From the FWHM of these profiles we derived the values given in Tbl. 1 for the coherence length r_0.

With the exception of the infrared measurement for phase-screen 2, all measured values are in very good agreement with the theoretically expected values. The use of two different wavelengths also allows us to determine whether the wavelength dependence of r_0 on the phase-screen substrate differs substantially from that expected in the Earth's atmosphere. Since the coherence length r_0 in the atmosphere scales as $\lambda^{1.2}$, we can compare with the ratio of r_0 determined at 632.8 and 831.5nm with that for the atmosphere (i.e. 0.72). All measurements are in agreement with the theoretically expected value within one standard deviation.

4.2. Point-spread functions demonstration videos obtained with MAPS

This section provides hyperlinks to three multimedia movies obtained with MAPS. The corresponding set-up parameters are listed in Tbl. 2. All videos were taken with a CCD camera positioned in the focal plane of MAPS. The videos nicely show the evolution of the atmosphere-

Table 1. Results of the r_0 measurement from direct imaging of the PSF.

phase-screen	$r_0(\lambda=632.8nm)$	$r_0(\lambda=831.5nm)$	r_0@632.8nm / r_0@831.5nm
PS1 computer template	0.44 ± 0.02mm	0.61 ± 0.02mm	0.72 ± 0.06
PS1 manufactured screen	0.43 ± 0.04mm	0.63 ± 0.03mm	0.68 ± 0.10
PS2 computer template	0.81 ± 0.03mm	1.12 ± 0.03mm	0.72 ± 0.05
PS2 manufactured screen	0.73 ± 0.06mm	1.11 ± 0.04mm	0.66 ± 0.08

Table 2. MAPS set-up parameters and MPEG demo movies.

Set-up parameter	demo #1	demo #2	demo #3
Pupil diameter D	13 mm	6.5 mm	6.5 mm
Wavelength	633 nm	633 nm	633 nm
PS1 position	ground-layer	ground-layer	ground-layer
PS1 wind speed	1.5 m/s	0.5 m/s	1.5 m/s
PS2 position	high-layer	high-layer	high-layer
PS2 wind speed	3.0 m/s	1.0 m/s	3.0 m/s
Total D/r_0	≈ 40	≈ 20	≈ 20
Long exposure seeing	0.6"	0.6"	0.6"
Speckle video frame rate	4 Hz	4 Hz	4 Hz
MPEG video size	2.3 MB	2.3 MB	2.3 MB
Link to movies	www.mpia.de	/homes/hippler/	SpeckleMovieX.mpg X=1,2,3

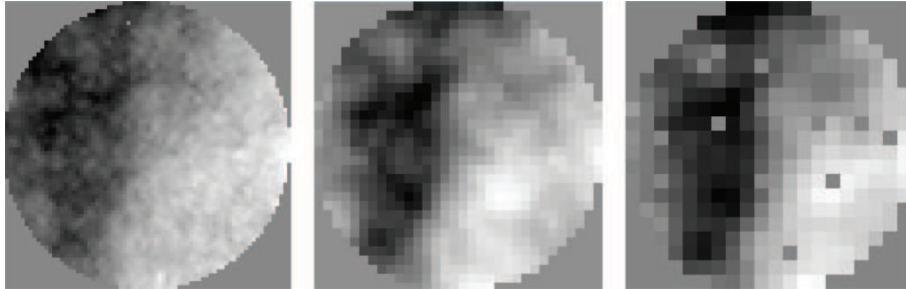like speckle pattern with time for various wind speeds and D/r_0 ratios.

Fig. 6. Examples of reconstructed phase maps of wavefronts using the AOA Shack-Hartmann wavefront sensor for three lenslet sizes, namely 133μm, 300μm, and 480μm (left to right). The isolated bad pixels visible in the right panel result from dirty lenslets.

4.3. Wavefront measurements

The wavefronts produced by the manufactured phase-screens were measured[1] with a commercial AOA Wavescope Shack-Hartmann sensor, using aperture sizes of typically $\sim$10mm

---

[1]We also attempted to make similar wavefront measurements using a phase-shifting Twyman-Green interferometer from FISBA, Switzerland. This was unsuccessful as the wavefront of the phase-screens could not be reconstructed by the interferometer.

and microlens arrays with 133, 300, and 480μm microlens diameter (pitch size). The phase-screens were illuminated with collimated light, using the HeNe laser and the infrared laser diode. In Fig. 6 we show the measured wavefront of the same location on phase-screen PS1, measured with the three available microlens arrays. They show a broadly similar low spatial
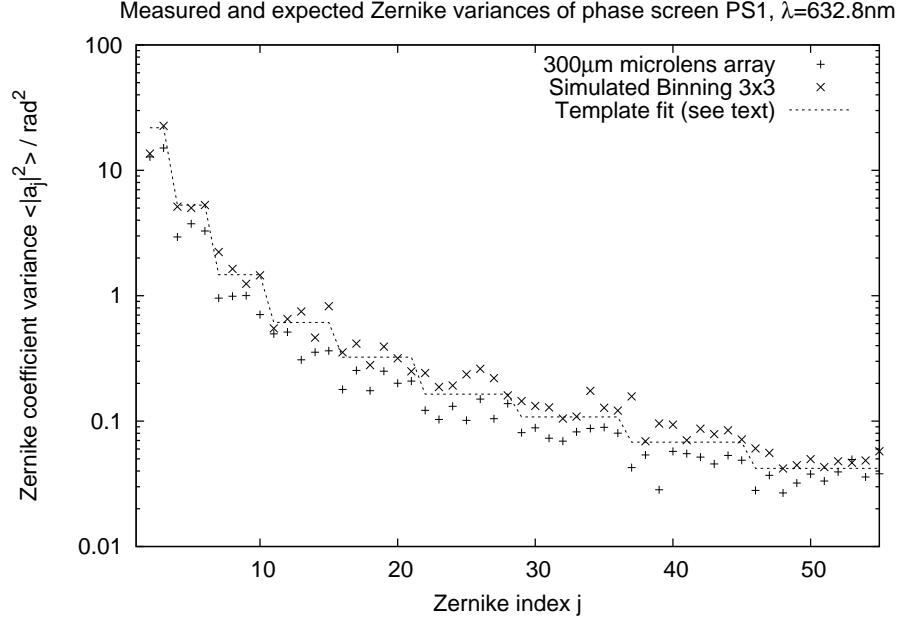
Measured and expected Zernike variances of phase screen PS1, λ=632.8nm

Fig. 7. Zernike coefficient variances of phase-screen PS1 at a wavelength of $\lambda = 632.8\mu$m. Measurements are based on Shack-Hartmann wavefront gradients obtained with the 300μm-lenslet array. The wavefronts of 100 randomly distributed test apertures with a diameter of 10mm were reconstructed with a least-squares Zernike decomposition. The plotted line (dashed) results from a fit to the Zernike variances calculated for the computer generated phase map under the assumption of a finite outer scale of L_0=22m. Zernike mode number 1 corresponds to the piston term and is omitted in the plot. A Zernike decomposition of the computer generated phase-screen with a 3 by 3 pixel binning corresponding to a cell size of 300μm is shown for comparison.

frequency structure, except for the left panel (i.e. using the 133μm-array), which appears to differ markedly. While it shows considerable fine structure, it also appears to be somewhat flatter than the other pair of phase maps. This is not unexpected if we recall that on one hand the Silios phase-screens have a square pixel-like structure, with each pixel, or cell, being (s_{cell}=) 100μm-wide. Yet, on the other hand, the Shack-Hartmann sensor only measures wavefront gradients, and that the minimum size of each lenslet used needs to be $> 2 \cdot s_{cell}$. It is therefore not surprising that the 133μm-array appears to be relatively insensitive to the wavefront shape.

In a quantitative approach, we decomposed both the measured wavefronts and the computer-generated phase maps into their Zernike representations and calculated the Zernike coefficient variances $< |a_j|^2 >$. In the case of the computer generated phase maps, the values were fitted accounting for a finite outer scale of L_0=22m. The expected and measured Zernike variances are shown in Fig.7 and Fig.8, considering all three different microlens arrays. Indeed, the Zernike coefficients variance measurements confirm that the 133μm-lenslet array (lenslet size $< 2 \cdot s_{cell}$) appears to be unsuitable for a statistical analysis of our phase-screens, as the vari-
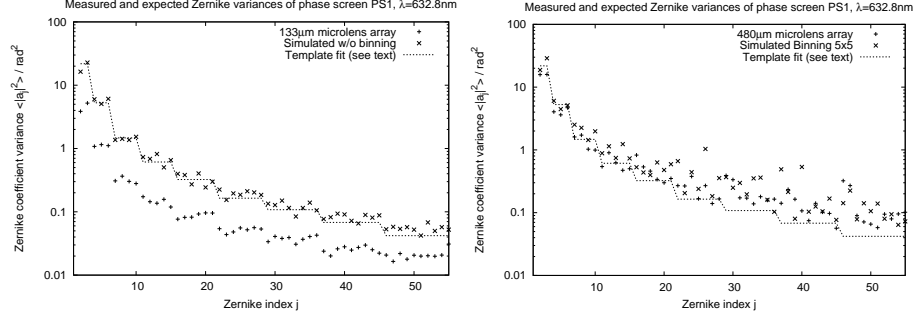
Fig. 8. Left: same as Fig. 7, but for the 133μm-lenslet array. A Zernike decomposition of the original computer-generated phase-screen (i.e. without additional pixel binning), corresponding to a cell size of 100μm, is shown for comparison. Right: Also the same as Fig. 7, but for the 480μm-lenslet array. A Zernike decomposition of the computer-generated phase-screen with a 5 by 5 pixel binning, corresponding to a cell size of 500μm, is shown for comparison.

ance estimated using the 133μm-array is considerably less than the expectation. As expected however the 300μm-array allows a better match to the numerical simulation. The variance data for the 480μm-array also provides a good match, except at Zernike indices above ~ 20, where there is increased scatter in $< |a_j|^2 >$, caused (at least in part) by the (relatively) small number of sampling elements (lenslets) available for constraining the high spatial frequencies on the phase-screen.

5. Conclusions

We have procured and characterized two phase-screens. We find that, within uncertainties, the statistical properties of both screens match those of the computer-generated templates. This suggests that the surface-etching technique allows reproducible phase-screens. In comparison to ion-exchange phase-screens [11] we conclude that phase-screens with small r_0 values (strongest optical turbulence) are more reliably produced with the etching technology. We want to note that Shack-Hartmann wavefront measurements of phase-screens with a discrete pixel-like fine structure require a minimum Shack-Hartmann lenslet diameter; this diameter has to be at least twice as large as the pixel size on the phase-screen.

Acknowledgments